

1 **Response of Coastal California Hydroclimate to the Paleocene-** 2 **Eocene Thermal Maximum**

3 Xiaodong Zhang^{1*}, Brett J. Tipple², Jiang Zhu³, William D. Rush⁴, Christian A. Shields³, Joseph
4 B. Novak⁵, James C. Zachos¹

5 ¹Department of Earth and Planetary Sciences, University of California, Santa Cruz, CA 95064, USA

6 ²FloraTrace Inc., Salt Lake City, UT 84103, USA

7 ³Climate and Global Dynamics Laboratory, National Center for Atmospheric Research, Boulder, CO 80307, USA

8 ⁴Department of Environmental Studies and Sciences, Santa Clara University, Santa Clara, CA 95053, USA

9 ⁵Department of Ocean Sciences, University of California, Santa Cruz, CA 95064, USA

10 *Correspondence to: Xiaodong Zhang (xzhan335@ucsc.edu)

11 **Abstract.** The effects of anthropogenic warming on the hydroclimate of California are becoming
12 more pronounced, with increased frequency of multi-year droughts and flooding. As a past
13 analog for the future, the Paleocene-Eocene Thermal Maximum (PETM) is a unique natural
14 experiment for assessing global and regional hydroclimate sensitivity to greenhouse gas
15 warming. Globally, extensive evidence (i.e., observations, climate models with high $p\text{CO}_2$)
16 demonstrates hydrological intensification with significant variability from region to region (i.e.,
17 dryer or wetter, or greater frequency and/or intensity of extreme events). Central California
18 (paleolatitude $\sim 42^\circ\text{N}$), roughly at the boundary between dry subtropical highs and mid-latitude
19 low pressure systems, would have been particularly susceptible to shifts in atmospheric
20 circulation and precipitation patterns/intensity. Here, we present new observations and climate
21 model output on regional/local hydroclimate responses in central California during the PETM.
22 Our findings based on multi-proxy evidence within the context of model output suggest a
23 transition to an overall drier climate punctuated by increased precipitation during summer
24 months along the central coastal California during the PETM.

25 **1 Introduction**

26 Global warming of a few degrees Celsius over the next century is projected to intensify the
27 hydrological cycle on a range of temporal and spatial scales, manifested primarily by amplified
28 wet-dry cycles (Held and Soden, 2006; Douville et al., 2021). Indeed, just over last few decades
29 there has been an increasing frequency in the severity of extremes characterized by compound
30 heat waves and intense drought (Büntgen et al., 2021; Williams et al., 2020; Zscheischler and
31 Lehner, 2022), and/or heavy precipitation and flooding (Liu et al., 2020; Risser and Wehner,
32 2017). As greenhouse gas driven warming continues, such precipitation extremes (wet or dry)
33 are expected to intensify (Stevenson et al., 2022). ~~This is particularly so for particularly in~~
34 ~~regions such as California which receives much of its rainfall from winter systems fueled by~~
35 ~~atmospheric rivers (AR), the frequency of which are forecast to decline as the systems shift~~
36 ~~northward (Simon Wang et al., 2017). The decline in winter precipitation along with warming~~
37 ~~will create more intense droughts even as the potential for extreme precipitation events increase~~
38 ~~(Vogel et al., 2020; Swain et al., 2018). receives much of its rainfall from winter systems fueled~~
39 ~~by atmospheric rivers (AR) the frequency of which are forecast to decline as the systems shift~~
40 ~~northward (Simon Wang et al., 2017). The drop in winter AR precipitation along with warming~~
41 ~~will create more intense droughts over much of the state even as the potential for extreme~~
42 ~~precipitation events increases (Vogel et al., 2020; Swain et al., 2018).~~

43 ~~California, a region vulnerable to amplified wet-dry cycles, is already experiencing multiyear~~
44 ~~extreme droughts with longer precipitation deficits interspersed with anomalously wet~~
45 ~~years (Zamora-Reyes et al., 2022). For example, the prolonged drought from 2012 to 2016~~
46 ~~preceded the exceptionally high numbers of atmospheric river storms related winter flooding of~~
47 ~~2017 (Simon Wang et al., 2017). Collectively, climate models (e.g., CESM, CMIP etc.) show that~~
48 ~~the occurrence of such extremes in droughts and excessive seasonal precipitation in California is~~
49 ~~expected to increase by the end of the century (Vogel et al., 2020; Swain et al., 2018). In addition,~~
50 ~~such ‘whiplash’ hydroclimate shifts related to anthropogenic warming are generally supported by~~
51 ~~historical records of California climate cycles (de Wet et al., 2021; Polade et al., 2017).~~

52 ~~The most robust evidence for gClimate model predictions for reenhouse warming-induced~~
53 ~~intensification of the hydrological cycle comes from are supported by global case studies of~~
54 ~~extreme~~ warming events of the deep past (Carmichael et al., 2017). In particular, the Paleocene-
55 Eocene Thermal Maximum (PETM) has emerged as a unique natural experiment for assessing

56 global and regional hydroclimate sensitivity to greenhouse gas warming (Zachos et al., 2008).
57 Extensive evidence exists for a major mode shift of local/regional precipitation patterns and
58 intensity (Pagani et al., 2006; Slotnick et al., 2012; Schmitz and Pujalte, 2003; Sluijs and
59 Brinkhuis, 2009; Smith et al., 2007; Handley et al., 2012; Kozdon et al., 2020) including
60 enhanced erosion and extreme flooding in fluvial sections (e.g., Pyrenees; Bighorn basin), and
61 increased weathering and sediment fluxes to coastal basins (e.g., Bass River, Wilson Lake, mid-
62 Atlantic coast; Mead Stream, New Zealand etc.) along with other observations (John et al., 2008;
63 Nicolo et al., 2010; Stassen et al., 2012; Self-Trail et al., 2017; Wing et al., 2005; Kraus and
64 Riggins, 2007; Foreman, 2014).

65 These observations of regional hydroclimate ~~change~~ serve as the basis for climate model
66 experiments forced with proxy-based estimates of $\Delta p\text{CO}_2$ for the PETM (i.e., 3x-6x pre-
67 industrial) (Kiehl and Shields, 2013; Carmichael et al., 2016; Zhu et al., 2020). Using such
68 estimates, model simulations show an overall increase in poleward meridional water vapor
69 transport as manifested by a net increase in evaporation of subtropical regions, balanced by
70 higher precipitation of tropical/high latitudes characterizing the ‘wet-gets-wetter and dry-gets-
71 drier’ hydrological response. The latest simulations using high-resolution climate models display
72 several key regional responses including increased frequency of extreme precipitation events,
73 especially the coastal regions where atmospheric rivers (AR) (~~AR~~) are common (Rush et al.,
74 2021). Indeed, observations of high-energy flooding events in SW Europe (i.e., the Pyrenees)
75 during the PETM (Schmitz and Pujalte, 2003) can be explained by increased frequency of North
76 Atlantic ARs contributing landfall in that region. Pacific AR activity as simulated for the PETM
77 also becomes more intense but less frequent along the central California coast by shifting
78 northward with the storm tracks (Shields et al., 2021), not unlike the projections for California in
79 the future (Shields and Kiehl, 2016; Massoud et al., 2019). This pattern is consistent with
80 warming scenarios in general which have weakened zonal wind belts (i.e., the westerlies) that are
81 shifting poleward (Abell et al., 2021; Douville et al., 2021).

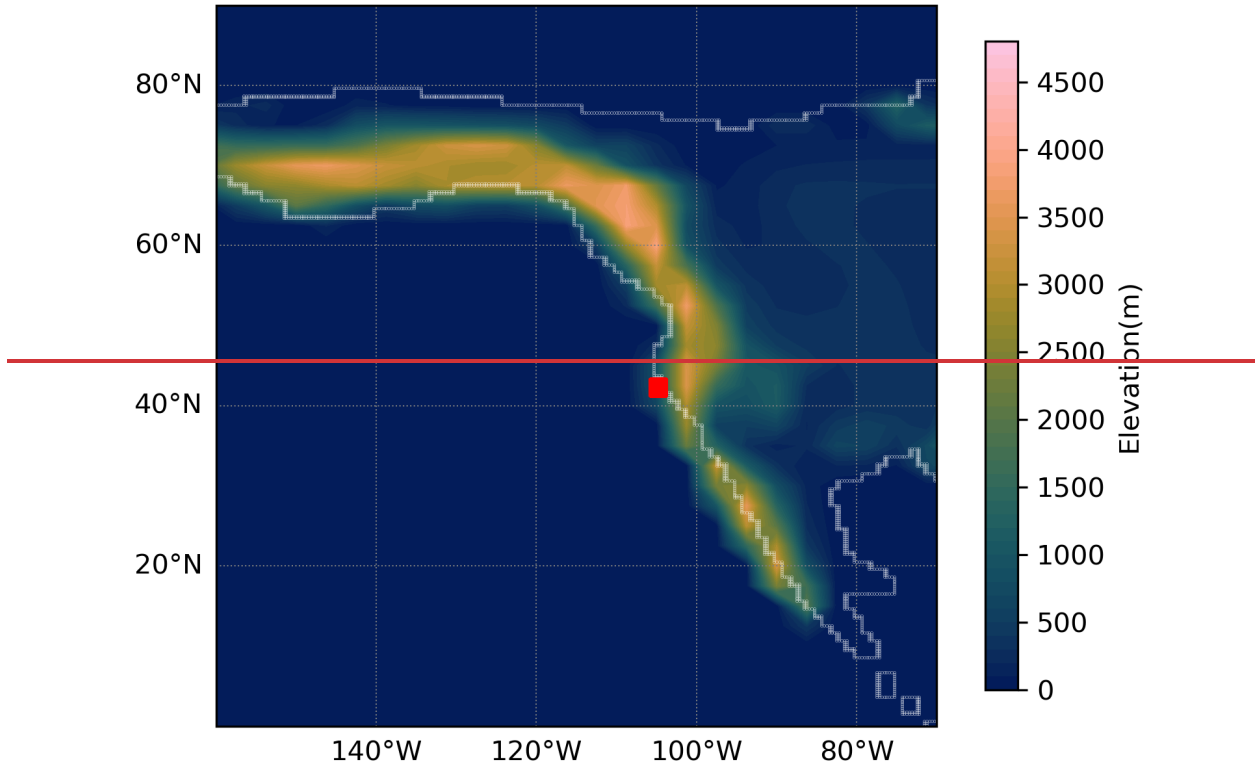
82 Testing the theoretical response of extreme global warming on Northeast Pacific ARs and
83 impacts on seasonal ~~seasonal~~ precipitation along North America’s western coast in general is
84 challenging and still limited by the lack of observations. Here we constrain the regional
85 hydroclimate response along the central California coast during the PETM using several

86 independent proxies (i.e., clay mineralogy, grain size distribution, $\delta^{13}\text{C}_{\text{org}}$ stratigraphy, and leaf
87 wax $\delta^2\text{H}_{n\text{-alkane}}$ isotope records), which are either directly or indirectly sensitive to shifts in
88 precipitation patterns/intensity. These proxies are then compared against ~~sophisticated~~ Earth
89 System model simulations ~~of the PETM climate to characterize~~ of the greenhouse gas forced
90 relative changes in regional precipitation (i.e., pattern/intensity). The new records complement
91 data from a previous study (John et al., 2008), and along with the latest climate modeling
92 experiments provide a unique case study of the sensitivity of regional hydroclimate to major
93 greenhouse warming.

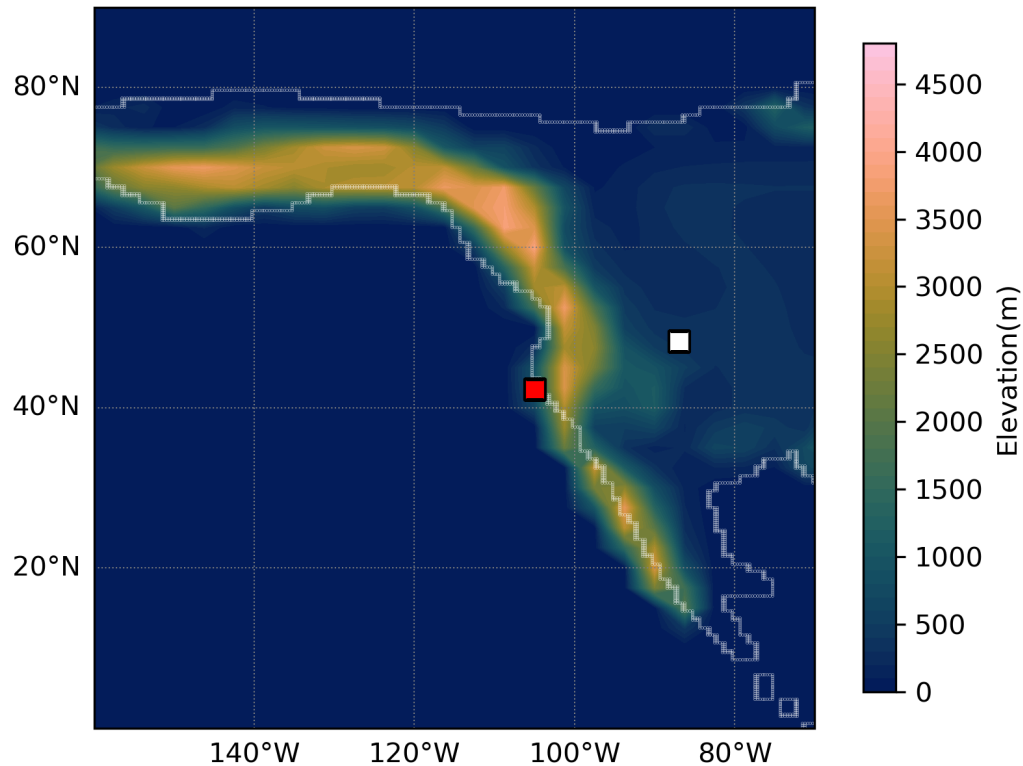
94 **2 Materials and methods**

95 2.1 Site Location

96 The studied outcrop section is part of the late Paleocene-early Eocene Lodo Formation located in
97 the Panoche Hill of central California (Fig. 1). During the late Paleocene, the section was
98 situated at a paleolatitude $\sim 42^\circ\text{N}$, roughly at the boundary between the dry subtropical highs and
99 mid-latitude low-pressure systems. The Lodo Formation is comprised primarily of siltstone with
100 a relatively low abundance of calcareous microfossils truncated by thin glauconitic sand layers
101 (Brabb, 1983). Depositional facies are consistent with neritic-bathyal setting along the outer
102 shelf (John et al., 2008).



103



104

105 Figure 1. Paleogeography and location of the Lodo Gulch section (red spot) along the Pacific coast
 106 and Big Horn Basin (white spot) in the North America continent for reference at 56 Ma.
 107 Late Paleocene-early Eocene topography boundary of North America was is adapted from Lunt
 108 et al. (2017). ~~Also show is the location of the Bighorn Basin section and ACEX.~~

109

110 2.2 Methods

111 2.2.1 Bulk organic sStable carbon isotopes

112 Sediment samples used for this study include those originally collected (ca. 28) by John et al.
 113 (2008). In addition, new samples (ca. 27) were collected from the upper Paleocene for organic C
 114 isotopic analyseis ($\delta^{13}\text{C}_{\text{org}}$) to better establish pre-PETM baseline. Samples were analyzed in the
 115 UCSC Stable Isotope Laboratory using a CE instruments NC2500 elemental analyzer coupled
 116 with Thermo Scientific Delta Plus XP iRMS via a Thermo-Scientific Conflo III. All samples

117 ~~were~~are calibrated with VPDB (Vienna PeeDee Belemnite) for $\delta^{13}\text{C}$ and AIR for $\delta^{15}\text{N}$ against an
118 in-house gelatin standard reference material (PUGel). Analytical reproducibility precision is \pm
119 0.1 ‰ for $\delta^{13}\text{C}$ and \pm 0.2 ‰ for $\delta^{15}\text{N}$.

120 2.2.2 Grain Size analysis~~is~~

121 Particle size was measured by laser diffraction using Beckman Coulter with Polarization
122 Intensity Differential Scatter (PIDS) housed at UCSC (see supplemental information). For each
123 sample, 2 to 5 mg of bulk ~~sediments was~~sediment was powered and sieved through 2-mm sieve
124 following the protocols in Blott et al., (2004) in each sample for measurement. A total of 39
125 samples were measured, e~~Each sample was performed 2 or 3 replicates in duplicate or triplicate~~
126 to ensure reproducibility.

127 2.2.3 Clay Assemblages analysis~~is~~

128 Sample preparation follows a slightly modified version of (Kemp et al., (2016). Roughly 5 to
129 10 g of sediment was powdered in a pestle and mortar and then placed in a Calgon (Sodium
130 hexametaphosphate) solution on a shaker table for 72 hours. Samples were sorted through a 63
131 μm sieve while collecting the fluid with the $<63\ \mu\text{m}$ fraction. The collected fluid and suspended
132 fine fraction ($< 63\ \mu\text{m}$) were allowed to settle for a period determined by Stokes' Law to keep $<$
133 2 ~~μm~~ μm size clay particles remaining in suspension. The fluid was then decanted and dried in the
134 oven at 40 °C. Approximately 150 mg clay of each sample were used to prepared oriented
135 mounts for X-ray diffraction (XRD) analysis. A total of 38 clay samples were prepared from the
136 Lodo Formation. The sample residues ~~were~~are measured on a Philips 3040/60 X'pert Pro X-ray
137 diffraction instrument at UCSC. Clay species (i.e., Smectite, Illite, Kaolinite, Chlorite) ~~were~~are
138 identified based on peak positions and intensities representing each clay mineral.

139 2.2.4 Leaf wax distribution and carbon/hydrogen isotopic composition

140 Sediment extraction, compound isolation, and compound-specific isotope measurements were
141 conducted following Tipple et al., (2011). Briefly, sediments were freeze-dried, powdered (\sim 500
142 g), and extracted with dichloromethane (DCM): methanol (2:1, v/v) using a Soxhlet extractor.
143 Total lipid extracts were concentrated and then separated by column chromatography using silica
144 gel. ~~Normal~~-alkanes were further purified from cyclic and branched alkanes using urea adduction

145 following (Wakeham and Pease, (2004). ~~Normal~~-alkane abundances were determined using gas
146 chromatograph (GC) with a flame ionization detector (FID). Isotope analyses were then
147 performed using a GC coupled to an ~~iRMS isotope ratio mass spectrometer~~ interfaced with a
148 GC-C III combustion system or a High Temperature Conversion system for $\delta^{13}\text{C}$ and $\delta^2\text{H}$
149 analyses, respectively. 35 samples were processed with a fused silica, DB-5 phase column (30 m
150 \times 0.25 mm I.D., 0.25 μm film thickness) with helium as the carrier at a flow of 1.5ml/min. GC
151 oven temperature program was 60-320°C @ 5°C/min and isothermal for 30 min. A Thermo
152 Trace MS was used for detection with the mass spec scanning from 50-800 m/z or exclusively
153 m/z of 191, 217, 218, 370, 372, 386, and 400 for single ion monitoring. Biomarkers were
154 identified by elution time and mass spectra of in-house petroleum standards with published
155 biomarker distributions (Peters et al., 2005).

156 $\delta^{13}\text{C}$ and $\delta^2\text{H}$ values are expressed relative to Vienna Pee Dee belemnite (VPDB) and Vienna
157 Standard Mean Ocean Water (VSMOW). Individual n-alkane isotope ratios were corrected to n-
158 alkane reference materials (for $\delta^{13}\text{C}$, C₂₀, C₂₅, C₂₇, C₃₀, and C₃₈ of known isotopic ratio and for
159 $\delta^2\text{H}$, “Mix A” from Arndt Schimmelmann, Indiana University) analyzed daily at several
160 concentrations. In addition, H₂ reference gas of known isotopic composition was pulsed between
161 sample n-alkane peaks to confirm if normalizations were appropriate. Standard deviations (SD)
162 of n-alkane reference materials were $\pm 0.6\text{‰}$ for $\delta^{13}\text{C}$ and $\pm 6\text{‰}$ for $\delta^2\text{H}$.

163 2.2.5 Earth System Models

164 ~~Two different set of e~~Climate simulations from two models -were used in this paper for (1)
165 comparison with leaf wax proxy data and (2) extreme events analyseis. (1) Water isotope-
166 enabled Community Earth System Model version 1.2 (iCESM1.2) simulates changes in climate
167 and water isotopic composition during the PETM (Zhu et al., 2020) with a horizontal resolution
168 of $1.9 \times 2.5^\circ$ in atmosphere and land, and a nominal 1 degree in the ocean and sea ice components.
169 Water isotope capabilities have been incorporated into all the components of CESM 1.2 (Brady
170 et al., 2019), which include the Community Atmosphere Model, version 5_(CAM5) for the
171 atmosphere, the Parellel Ocean Program, version 2_(POP2) for the ocean, the Community Land
172 Model, version 4_(CLM4) for the land, River Transport Model (RTM) for river flow, and
173 Community Ice Code, version 4 for sea ice. All simulations were run with the identical boundary
174 conditions (including early Eocene paleogeography, land-sea mask, vegetation distribution, and

175 pre-industrial (PI) non-CO₂ greenhouse gas concentrations, soil properties, natural aerosol
176 emissions, solar constant and orbital parameters) following the DeepMIP protocol (Lunt et al.,
177 2017) and differ only in atmospheric CO₂ concentration. Crucially, the models with reduced
178 latitudinal temperature gradients (e.g., GFDL, CESM) more closely reproduce proxy-derived
179 precipitation estimates and other key climate metrics (Cramwinckel et al., 2022). Increased
180 climate sensitivity with warming and cloud feedback in CESM1.2 over earlier models improved
181 water vapor sensitivity. (2) Using the same CESM1.2 framework, high resolution (0.25°)
182 simulations were conducted with forced sea surface temperatures (SSTs) and active atmosphere
183 and land components (CAM5, CLM4). RTM was run at 1° resolution, and forced SST were
184 calculated from consistent 2° fully coupled PETM simulations (see details in Rush et al., 2021
185 and reference therein). The much higher horizontal resolution in the atmosphere enables
186 improved simulation of the extreme events. Hourly, daily (CAM5), and monthly (iCESM1.2)
187 temporal resolution precipitation outputs from both sets of climate simulations were utilized in
188 this paper, with 100 years taken from the equilibrated iCESM1.2 simulations, and 15 years from
189 the forced SST high resolution CAM5 simulations.

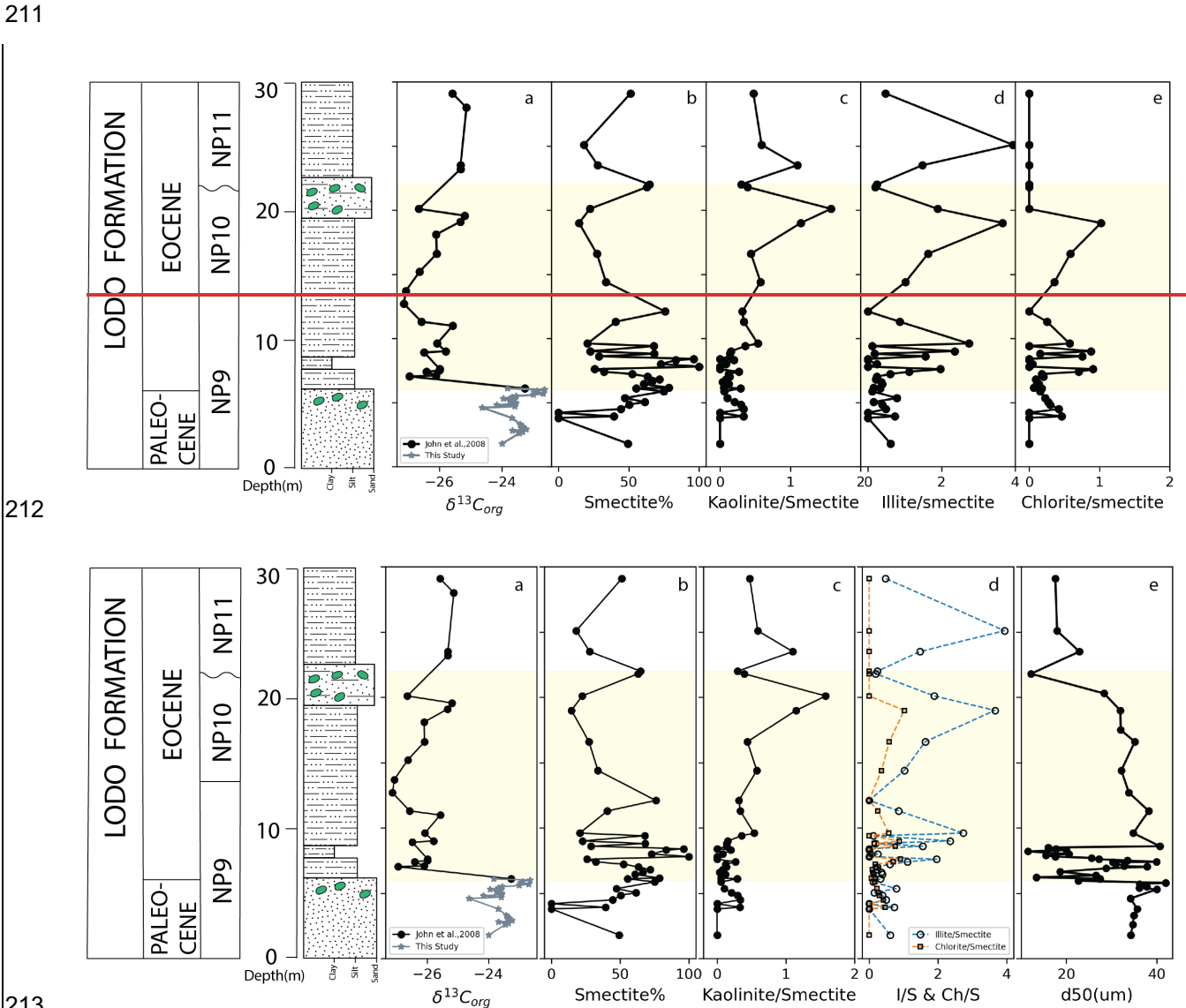
190

191 **3 Results**

192 3.1 Bulk organic and *n*-alkane stable cCarbon isotopes

193 A carbon isotope excursion is present in both bulk organic (Fig. 2a) and carbonate based $\delta^{13}\text{C}$
194 records (John et al., 2008) across the P-E boundary (Fig. 2a), marking the PETM onset of the
195 Lodo section (John et al., 2008). The terrestrial leaf wax *n*-alkane records all captures the carbon
196 isotope excursion (CIE) with a pattern that roughly parallels the other published records (i.e.,
197 planktonic foraminifera) (John et al., 2008), though is much less noisy than the bulk C_{org} record,
198 not unexpected given the potentially variable composition of the bulk organic matter. The
199 magnitude of the $\Delta\text{-}\delta^{13}\text{C}_{n\text{-alkane}}$ change is roughly is roughly -4‰ (average of n-C₂₇, n-C₂₉, n-C₃₁)
200 at the onset of the CIE, followed by a gradual recovery that is truncated at the disconformity
201 between 20.3m and 23.5m (coincides with nannofossil biozone boundary NP10 and NP11), thus
202 marking the top of the PETM body (Fig. 2a3b). The disconformity likely coincides with a global
203 sea level regression as recorded in other shallow marine sections (John et al., 2008). This
204 disconformity between 20.3 and 23.5m is also marked by nannofossil biozone boundary between
205 NP10 and NP11 both in organic carbon and *n*-alkane carbon isotopes. The main biostratigraphy

206 datum identified at the NP9-NP10 boundary at 14.4m, which corresponds to CIE recovery
 207 interval. In the upper Lodo Formation above 20m Following the recovery, above the
 208 disconformity, the mean $\delta^{13}C_{n-alkane}$ $\delta^{13}C_{org}$ is relative enriched is compared to the PETM body
 209 but more depleted to relative to the pre-PETM baseline which also as is -observed in other most
 210 other PETM sections (Tippie et al., 2011; Handley et al., 2012).

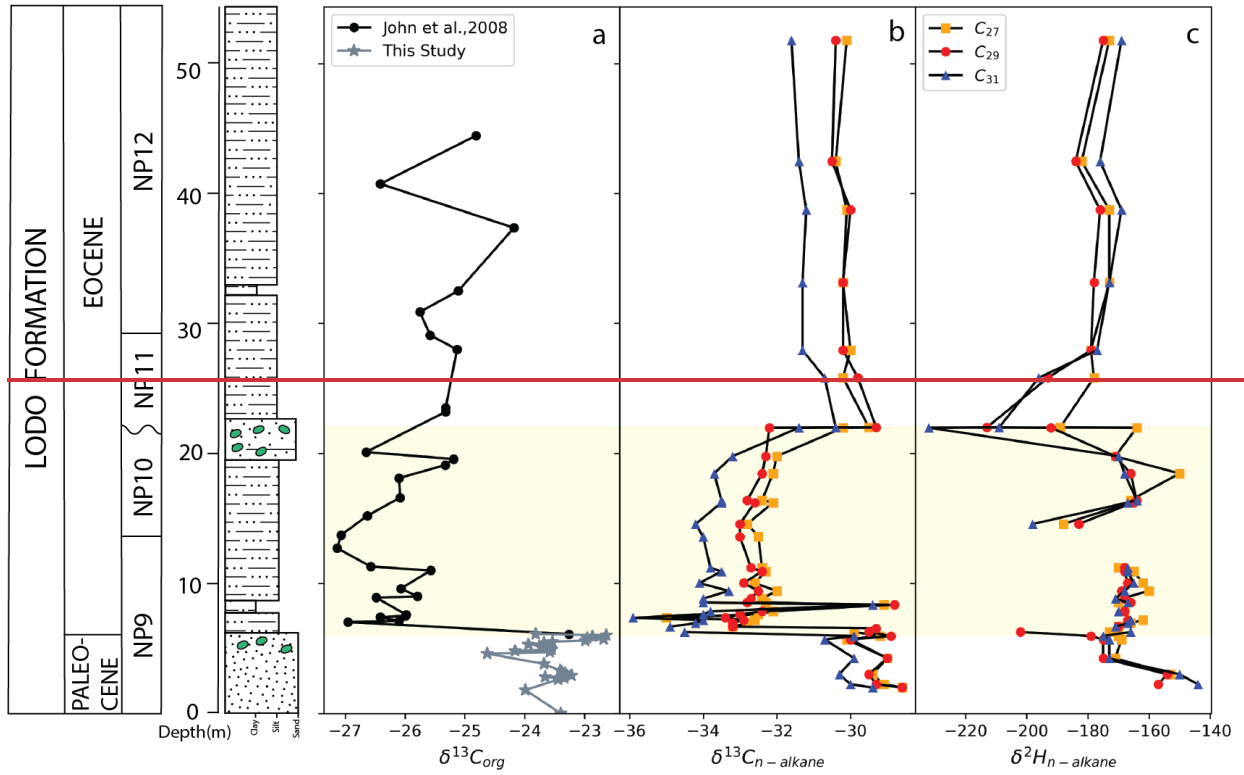


214 Figure 2-3 Integrated C isotope and clay assemblage records of Lodo Fm in the Lodo Gulch of
 215 central California (a) bulk organic carbon isotope, (b,c,d,e) clay assemblage ratios, (e) decreasing
 216 mean particle size (d50: 50% of the total particle size in sediments) corresponds to CIE onset. -

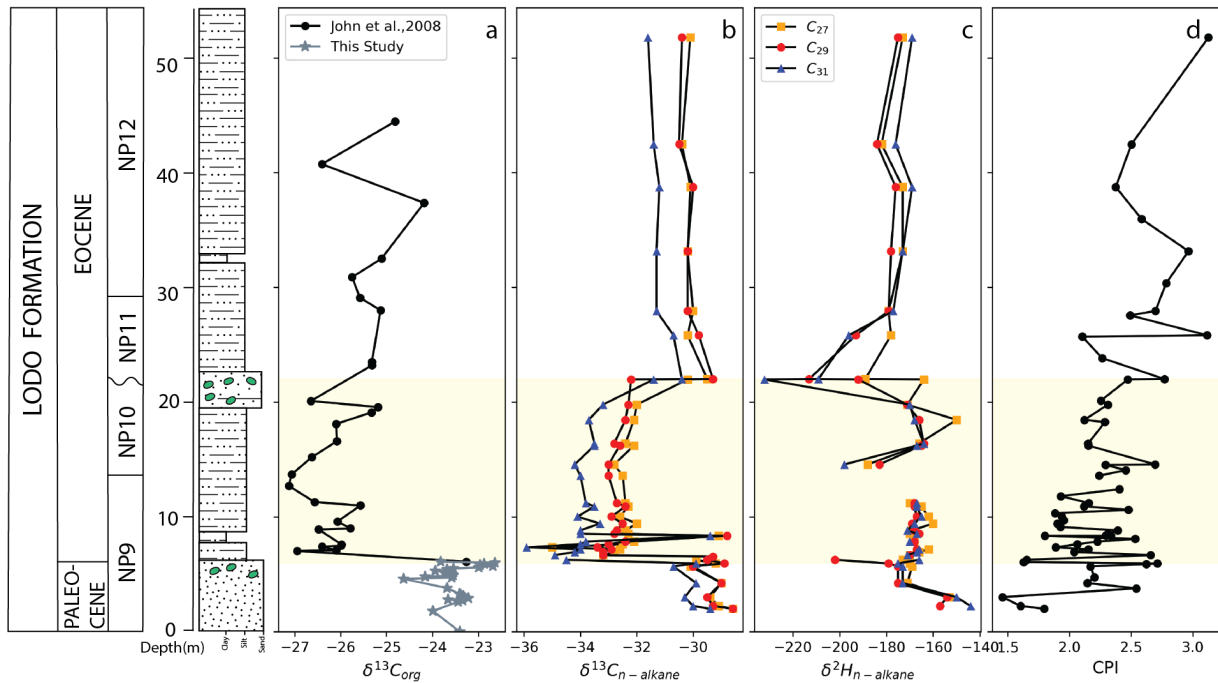
218
219
220
221
222
223
224
225
226
227
228
229
230
231
232
233
234
235
236
237
238
239
240
241
242

3.2 Hydrogen isotopes

The leaf wax $\delta^2\text{H}_{n\text{-alkane}}$ values range from -150 to -213‰ over the entire sampled section has with an initial decrease by of 25‰ (from -150 to -175‰ in C_{29}) just prior to the CIE onset followed by a slight enrichment of in the main body PETM and then followed by a slight rise (Fig. 23c). This negative shift recorded in the coarse sandy facies of Lodo Formation in the late Paleocene, although limited sample size (ca. 2) could bias the trend, similar magnitude of leaf wax $\delta^2\text{H}_{n\text{-alkane}}$ but increase prior to the PETM observed in other sections (Handley et al., 2008, 2011; Jaramillo et al., 2010; Tipple et al., 2011). Across P-E boundary around 6.1 m, there is slight enrichment (~6 ‰) of $\delta^2\text{H}_{n\text{-alkane}}$ into the right just after the onset main body PETM. The relatively invariable $\delta^2\text{H}_{n\text{-alkane}}$ through the PETM is punctuated with one or two brief intervals of more negative values with one right across the onset and the other nearby initial recovery (-202‰ at 6.26m and -213‰ at 22m). The second larger anomaly coincides with the disconformity (related to local sea level regression). Compared to The post-PETM $\delta^2\text{H}_{n\text{-alkane}}$ values, pre-PETM $\delta^2\text{H}_{n\text{-alkane}}$ are on average lower than for the upper Paleocene/PETM is relatively enriched. -Given the limited number of samples to establish a baseline for the upper Paleocene, the significance of the pre (and post CIE) shifts/anomalies in $\delta^2\text{H}_{n\text{-alkane}}$ should be considered with some caution. Several similar magnitude of leaf wax $\delta^2\text{H}_{n\text{-alkane}}$ but increase prior to the PETM observed in other sections do show pre-CIE shifts, both positive and negative, and typically an enrichment with the CIE (Handley et al., 2008, 2011; Jaramillo et al., 2010; Tipple et al., 2011). Across Such minor changes likely reflect unconstrained orbital influences on regional precipitation (Rush et al., 2022; Campbell et al., 2024), especially considering that the variable direction of change from location to location.



243



244

245 Figure 23. Marine $\delta^{13}\text{C}$ and Terrestrial higher plant leaf wax n-alkane $\delta^{13}\text{C}$ and $\delta^2\text{H}$ records.

246 Yellow shaded area represents The shaded area represents the bounds of the CIE/PETM (a) bulk

247 organic carbon isotope record of Lodo Fm. (b,c) leaf wax compound specific carbon/hydrogen

248 isotope records in n -C₂₇ (yellow square), n -C₂₉ (red closed circle), n -C₃₁ (blue triangle), and n -
249 alkane carbon preference indices (CPI).

250

251 3.3 Clay Assemblage and grain Size

252 Clay assemblages and particle grain size should to some extent be influenced by regional
253 hydroclimate. At Lodo, the clay assemblage data (Fig. 32) shows are dominated by smectite
254 smectite dominated in the Lodo Formation during PETM throughout, along with increasing. The
255 minor clay components illite and smectite and chlorite/smectite ratios show several spikes
256 relative to smectite within the lower (8 to 10 m) and upper CIE (~19 m), whereas the ratio of
257 kaolinite gradually increases (0.5 to 1.5) only over the upper portion of the CIE (10 to 20 m). A
258 delayed rise in kaolinite has also been observed in a few other PETM sections whereas some
259 show an immediate rise (Tateo, 2020; Gibson et al., 2000). Gradually increase of the smectite
260 during the CIE corresponds to increase sedimentation rate. The smectite concentration and
261 kaolinite/smectite ratio stays remain high in the post-PETM interval compared to pre-PETM.
262 The late Paleocene of Lodo Formation lower Lodo Formation, with relative coarse sandy size,
263 shows slight spikes of kaolinite associated with other minerals. Grain size, largely silt and clay,
264 shows a distinct shift toward finer fractions (i.e., clay) with the onset of the CIE (Fig. 3eS4).

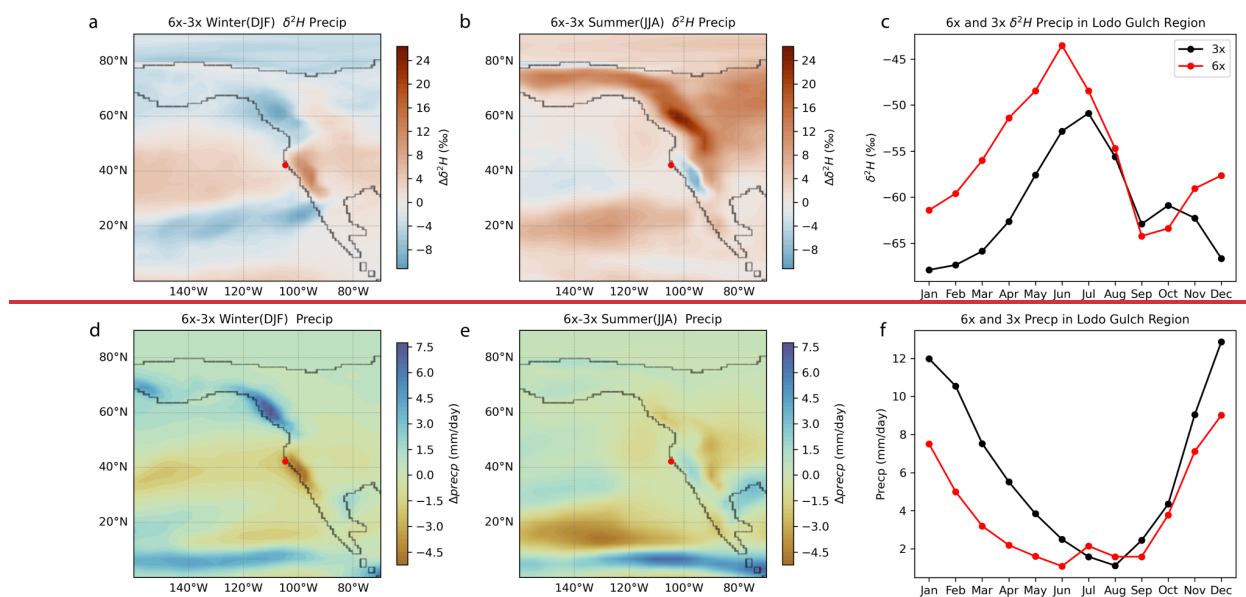
265

266 3.4 Earth system model simulations

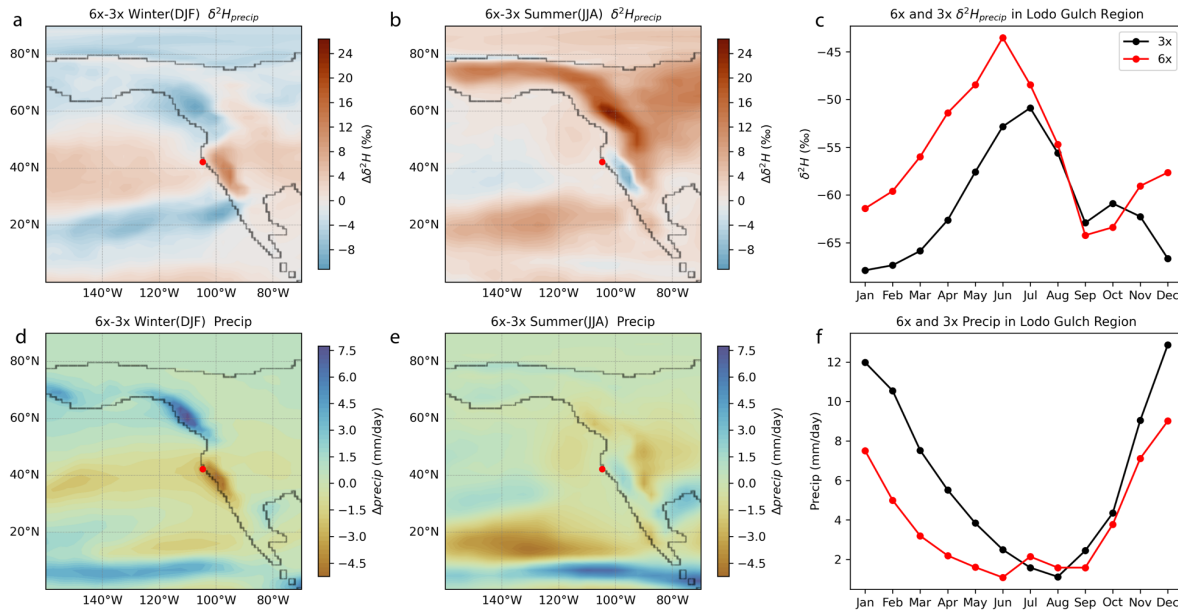
267 Precipitation We obtained and processed temperature and precipitation output from from two
268 community earth system/climate models: the isotope enabled iCESM1.2 under enhanced
269 greenhouse gas simulations (1x, 3x, 6x, 9x pCO₂ pre-industrial) and the high-resolution CAM5
270 models (daily precipitation over 15 years) forced by under a range of greenhouse conditions
271 (1x, 3x, 6x, 9x pCO₂ pre-industrial), both with Eocene paleogeography, were analyzed. For this
272 study comparisons with observations, we used used output from the 3x to 6x pCO₂ forcing
273 simulations that which best replicate the observed ASST (Δ SST) from for the pre-PETM and to
274 PETM (Zhu et al., 2020). Overall, monthly winter precipitation for the study region decreases
275 (~30%) during the PETM in both simulations but with a slight increase in the summer (Fig. 4,5).
276 CAM5 output shows a modest decrease in mean annual precipitation with significant seasonal
277 shifts during the PETM (Fig. 5a). Seasonal changes of monthly averaged $\delta^{18}\text{O}$ and $\delta^2\text{H}$ from
278 mean monthly precipitation (MAP) in iCESM1.2 of central California are consistent with

279 CAM5. On average the $\delta^2\text{H}_{\text{precip}}$ increases by ca. 5-10 ‰ from pre-PETM to PETM, especially in
 280 the winter/spring, with a smaller shift in summer/fall (1~2 ‰) (Fig 4. a,b,c). The Extreme value
 281 index (ξ), a representation of the distribution of exceedance right tail (supplemental information),
 282 shows a small but statistically robust increase in wet extremes of winter (DJF) with a significant
 283 increase in summer (JJA) wet exceedances during the PETM in the precipitation output from
 284 CAM5 simulations (Fig. 5b).

285



286



287

288

289

290

291

292

293

294

295

296

297

298

299

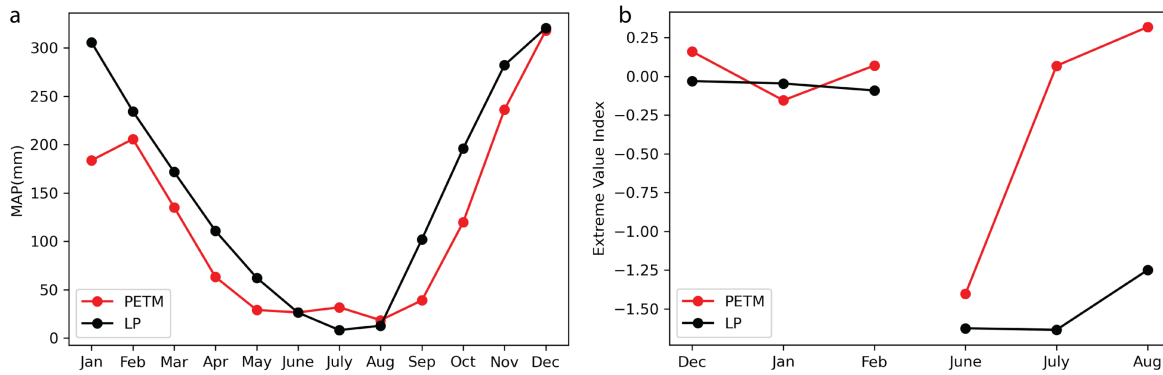
300

301

302

303

Figure 4. Seasonal and monthly meteoric precipitation amounts (mm/day) and H-isotopic composition for the North Pacific/Western N. America as simulated with the Water isotope-enabled iCESM1.2 model output (Zhu et al., 2020) of monthly hydrogen isotope record of meteoric precipitation under different pCO₂ forcing to pre-PETM industry (3x in black) represents pre-PETM, PETM(6x in red) pCO₂ forcing represents PETM) in east Pacific coast (red spot represents the Lodo Gulch study site). The iCESM1.2 simulations used the DeepMIP boundary conditions (Lunt et al., 2017). Panels (a) and (b) show $\Delta \delta^2H_{precip}$ Difference in between pre-PETM(3x) and PETM(6x) in winter (DJF a) and summer (JJA b) hydrogen isotope composition between pre-PETM(3x) and PETM(6x). Panel (c) shows the annual seasonal cycle of δ^2H_{precip} hydrogen isotope composition of precipitation at in Lodo Gulch (pre-PETM in black, PETM in red) region. Mean daily precipitation rate difference for in winter (d) and summer (e) precipitation amount between pre-PETM(3x) and PETM(6x) in east Pacific coast. Panel (f) shows the annual seasonal cycle of daily precipitation rate amount at in Lodo Gulch region. Site V values of Lodo Gulch region are calculated by represent the area-weighted average over 4° x 4° box around bounding the study site.



304

305 Figure 5. (a) High resolution CAM5 model output (Shields et al., 2021) of (a) mean monthly
 306 precipitation at Lodo over 15 model years in central coastal California regions during pre-PETM
 307 (for the Late Paleocene/LP) under low pCO_2 (680 ppmv) and PETM under high pCO_2
 308 (1590ppmv). (b) Extreme value index (ξ) comparison results of mean monthly precipitation in
 309 winter and versus summer of central coastal California region.

310

311 4 Discussion

312 4.1 Hydroclimate response from model simulations

313 In all model simulations of the PETM forced with higher pCO_2 (e.g., 3x to 6x pre-industrial), the
 314 hydrological cycle during PETM intensifies as manifested by increases in global mean
 315 precipitation and meridional vapor transport (Kiehl and Shields, 2013; Kiehl et al., 2018;
 316 Carmichael et al., 2016; Zhu et al., 2020). Regionally however, the magnitude and even the sign
 317 of precipitation change can differ considerably from global means (Carmichael et al., 2016,
 318 2017). This is most evident in the latest low and high-resolution model simulations of the PETM
 319 (Zhu et al., 202; Shields et al., 2021). For central California, the simulations yield modest an
 320 overall decline changes in mean annual precipitation but mainly due to significant seasonal shifts
 321 with a notable decline in winter precipitation with only and a slight increase in summer (Fig. 4).
 322 This pattern is produced by both the water isotope enabled iCESM1.2 and the higher resolution
 323 CAM5 with an overall shift into lower amplitude seasonal cycles as (i.e., a drier winter/spring
 324 and a slightly wetter summer) (Fig. 4, 5). This seasonal wet-dry shift appears to be driven in part
 325 by a pronounced northward shift of atmospheric rivers (ARs) in winter along the North
 326 American Pacific coastline (Shields et al., 2021). As Given the ARs delivering most the majority
 327 of winter precipitation to the mid-latitude Pacific coast, less frequent AR occurrences would

328 result in relatively drier winters during the PETM. Moreover, the extreme value index (ξ) shows
329 a small but statistically robust increase in winter (DJF) wet extremes with a significant increase in
330 the probability of summer (JJA) wet exceedance during PETM (Fig. 5b). Although AR-related
331 coastal winter storms reduced in frequency (Shields et al., 2021), the latter might be due
332 summer precipitation increased in intensity thus potentially enhancing individual extremes in this
333 region, possibly related to elevated an increase in summer tropical storm activity along the Pacific
334 coast during PETM (Fig. S74 Kiehl et al., 2021).

335 4.2 Hydroclimate response from observations

336 4.2.1. Sedimentation rate, clay assemblages and grain size distribution

337 Independent-Arguably, the collection of proxies observations from Lodo (i.e., sediment flux, clay
338 assemblages, and leaf wax water $\delta^2\text{H}$ isotopes ($^2\text{H}/^1\text{H}$ or $^{18}\text{O}/^{16}\text{O}$), though each has within
339 limitations, appear to be mostly consistent with the model output. collectively can contribute
340 toward a general picture of how the mode of precipitation changed (i.e., wetter or dryer, and/or
341 greater seasonality or extremes). For central California, model simulations of the PETM with
342 low and high resolutions exhibit an overall decrease in mean annual precipitation (Fig. 4,5). For
343 a mountainous coastal environment (Fig. 1), starting with siliciclastic sedimentation, rates rates
344 should be highly susceptible to a major shift in hydrologic conditions changes among other
345 factors. In addition to relief and lithology, as the changes in the seasonality of precipitation (and
346 along with vegetation vegetative cover) would be major controls on impact rates of erosion and
347 siliciclastic sediment flux transport. However, constraining The coarse resolution of
348 stratigraphic control at Lodo does limit the ability to constrain changes in sedimentation rates in
349 detail in shelf sections is challenging given the limitations of chronostratigraphy in such facies.
350 Previous studies by John et al., (2008) has established carbon isotope stratigraphy As such,
351 mainly based we rely largely on biostratigraphic constraints, with carbon isotope stratigraphy
352 However, As the CIE is well captured in both organic and inorganic (calcite) fossil materials in
353 Lodo just considering the thickness of the CIE (~10 m), one could argue for a shift toward higher
354 seasonality of precipitation with overall drier conditions as suggested by (John et al.,
355 (2008). This expanded CIE interval indicates higher sedimentation rates during the PETM (John
356 et al., 2008). Sedimentation rates on the continental shelf margin are highly sensitive to

357 ~~terrestrial sediment discharge and relative sea-level change. Assuming the latter was relatively~~
358 ~~static or rising (Sluijs et al., 2008), the higher sedimentation rates suggest increasing sediment~~
359 ~~supply from river runoff to the continental margin, reflecting a mode shift in regional~~
360 ~~hydroclimate.~~

361

362 ~~The other constraints on regional precipitation would also support a shift toward drier conditions.~~

363 4.1 Hydroclimate response from clay mineralogy

364 ~~Clay assemblages in nearshore settings can reflect physical and chemical weathering changes as~~
365 ~~influenced by regional climate change. Indeed~~For example, an increase in the relative abundance

366 of kaolinite fluxes has been widely observed across the CIE onset in many PETM sections from
367 mid to high latitudes (Tateo, 2020; Gibson et al., 2000) and interpreted as evidence of a major
368 mode shift in local hydroclimates. In contrast, the clay mineralogy (Fig. 3) for the Lodo

369 Formation is dominated mainly by smectite at the onset of the PETM, consistent with seasonal
370 wet/dry cycles under warm conditions (Gibson et al., 2000). A subtle increase in the

371 kaolinite/smectite ~~hints slightly enhanced~~could be interpreted as evidence of higher humidity,
372 ~~possibly related to enhanced seasonally subtropical conditions~~(Foreman, 2014). However, Such

373 ~~inferences of hydroclimate changes in the context of coastal deposition are complicated by~~

374 ~~fluvial runoff conditions (i.e., provenance, discharge, sediment influx) and precipitation (i.e.,~~

375 ~~seasonal vs mean annual).~~ the sSkewed grain size distribution of clay sediments around 8m

376 coinciding with illite/~~smectite~~kaolinite peaks (Fig. 3e and S1) indicates higher fluvial velocity

377 and increased erosion as observed ~~in other locations~~elsewhere (Chen et al., 2018; Foreman et al.,

378 2012; Foreman, 2014). For example, along the mid-Atlantic margin it appears the kaolinite might

379 have been exhumed from local Cretaceous ~~age~~-laterites (Lyons et al., 2018). This enhanced

380 physical weathering and erosion at Lodo could be related to an increase in episodic wet/dry

381 extremes as seasonality intensified during the PETM. ~~The lower Lodo Formation, with relative~~

382 ~~coarse sandy size distribution preceding the PETM, shows a slight pulse of kaolinite associated~~

383 ~~with other minerals, possibly indicating an early change of hydrological condition in the latest~~

384 ~~Paleocene before the PETM as observed elsewhere (Rush et al., 2021). The CIE onset likely~~

385 ~~represents a transient response to warming-induced hydroclimate changes, whereas the pre-~~

386 ~~PETM shift as well as minor variations post-CIE onset are likely orbitally forced (Kiehl et al.,~~

387 ~~2018; Campbell et al., 2023).~~

388
389
390
391
392
393
394
395
396
397
398
399
400
401
402
403
404
405
406
407
408
409
410
411
412
413
414
415
416

4.2.2 Precipitation and Leaf wax $\delta^2\text{H}_{n\text{-alkane}}$

The Lodo leaf wax $\delta^2\text{H}_{n\text{-alkane}}$ record at first glance is somewhat equivocal in terms of with respect to the modeling and overall response of local hydroclimate. In theory,

4.2 Hydroclimate response from earth system simulations

~~In all model simulations forced with higher pCO₂ (e.g., 3x to 6x pre industrial), the hydrological cycle during PETM intensifies as manifested by increases in global mean precipitation and meridional vapor transport (Kiehl and Shields, 2013; Kiehl et al., 2018; Carmichael et al., 2016; Zhu et al., 2020). Regionally however, the magnitude and even the sign of precipitation change can differ considerably from global means. This is most evident in the latest low and high-resolution model simulations of the PETM. For central California, the simulations yield modest changes in mean annual precipitation but significant seasonal shifts with a notable decline in winter precipitation and a slight increase in summer (Fig. 4). This pattern is produced by both the water isotope enabled iCESM1.2 and the higher resolution CAM5 with an overall shift into lower amplitude seasonal cycles as a drier winter/spring and a slightly wetter summer (Fig. 4, 5). This seasonal wet-dry shift appears to be driven in part by a pronounced northward shift of atmospheric rivers (ARs) in winter along the Pacific coast (Shields et al., 2021). Given the ARs delivering the majority of winter precipitation to the mid-latitude Pacific coast, less frequent AR occurrences would result in relatively drier winters during PETM. Moreover, the extreme value index (ξ) shows a small but statistically robust increase winter (DJF) wet extremes with a significant increase in the probability of summer (JJA) wet exceedance during PETM (Fig. 5b). Although AR-related coastal winter storms reduced in frequency (Shields et al., 2021), summer precipitation increased in intensity thus potentially enhancing individual extremes in this region, possibly related to an increase in summer tropical storm activity along the Pacific coast during PETM (Fig. S4).~~

4.3 $^2\text{H}/^1\text{H}$ composition of leaf waxes.

~~Terrestrial archives exhibit considerable evidence of environmental response to intensified hydrological cycle during the PETM (McInerney and Wing, 2011). In western North America, plant fossils show widely expansion (up to 40°N) of tropical rainforest during the PETM along~~

417 ~~the east Pacific in mid-latitude (Willis, K.J., McElwain, 2002; Korasidis et al., 2022).~~ Terrestrial
418 higher plant ~~hydrogen isotope composition (i.e., $\delta^2\text{H}_{n\text{-alkane}}$)~~ provide evidence ~~should provide~~
419 ~~insight into -changes in for regional mode shifts of precipitation amounts/source, particularly~~
420 ~~major mode shifts~~ (Handley et al., 2008, 2011; Jaramillo et al., 2010; Pagani et al., 2006; Tipple
421 et al., 2011). ~~Generally~~ ~~In some PETM records,~~ $\delta^2\text{H}_{n\text{-alkane}}$ significantly increases ~~in most of~~
422 ~~these records as expected with,~~ consistent with the effects of higher ~~warming T~~ on water isotope
423 ~~fractionation. For example, high latitudes in the Arctic,~~ $\delta^2\text{H}_{n\text{-alkane}}$ records show a positive
424 ~~excursion of 55‰ at CIE onset during PETM, consistent with a higher T,~~ reduced meridional
425 ~~temperature gradient and decreasing isotope distillation during vapor transport (Pagani et al.,~~
426 ~~2006).~~ However, ~~ther,~~ ~~but regionally,~~ notable similarities and differences ~~existe~~ are notable
427 ~~exceptionse~~d. In ~~some~~ ~~several~~ subtropical/mid-latitude ~~regions~~ sites, $\delta^2\text{H}_{n\text{-alkane}}$ increases prior to the
428 PETM followed by a ~~decreases~~ large negative excursion (ca ~20‰) across the onset of PETM
429 (Handley et al., 2008, 2011; Jaramillo et al., 2010; Tipple et al., 2011). ~~In sharp contrast, high~~
430 ~~latitudes $\delta^2\text{H}_{n\text{-alkane}}$ show a positive excursion of 55‰ at CIE onset during PETM, consistent with~~
431 ~~a reduced meridional temperature gradient and decreasing isotope distillation during vapor~~
432 ~~transport (Pagani et al., 2006).~~ However, ~~the~~ ~~In comparison,~~ Lodo $\delta^2\text{H}_{n\text{-alkane}}$ displays a
433 comparatively muted response, ~~initially decreasing by 25‰ just prior to the CIE onset followed~~
434 ~~by~~ showing a slight ^2H enrichment in the main body PETM followed by several ~~anomalous~~ shifts
435 toward more negative values (Fig. 23c). ~~The shift to more negative $\delta^2\text{H}_{n\text{-alkane}}$ values prior to the~~
436 ~~onset of CIE in Lodo likely represents background variability related to orbital forcing which~~
437 ~~also observed in other hyperthermal event (i.e., EECO) (Campbell et al., 2023; Walters et al.,~~
438 ~~2023.)~~
439
440 ~~Inferring and comparing the hydroclimate response from leaf water $\delta^2\text{H}$ at any location can be~~
441 ~~complicated. This muted hydrological response from~~ Given the robust evidence for ~~mode~~ ~~a~~ ~~major~~
442 ~~shifts in hydroclimate elsewhere during the PETM, does the relatively stable Lodo $\delta^2\text{H}_{n\text{-alkane}}$~~
443 ~~record leaf wax n -alkanes in Lodo cannot be simply interpreted as~~ necessarily support a
444 ~~locally/regional stable hydroclimate conditions during the PETM (i.e., in conflict with the~~
445 ~~modeling and other observations)?~~ since models and published proxy records suggest opposite
446 ~~interpretation when higher frequency extreme rainfall events inferred during the PETM~~
447 ~~(Carmichael et al., 2016, 2017; Rush et al., 2022)~~ Hydrogen-As H-isotope fractionation in plants is

448 ~~tightly~~ related to photosynthetic pathways, source water availability, and atmospheric humidity
449 (Sachse et al., 2012; Tipple et al., 2015), ~~it's possible that local shifts in meteoric water isotope~~
450 ~~composition were offset by another influencing factor(s).~~ ~~Along~~ Regarding photosynthetic
451 ~~pathways, along~~ the west coast of North America, no detailed records of vegetation response
452 have been generated for the PETM. ~~Still, for the longer term late Paleocene and early Eocene~~
453 ~~intervals, Lack of change in average chain length (ACL) (Fig S3) consistent with Korasidis et al.~~
454 ~~(2022), suggest little found little changedeviation in the Koppen-Geiger climate type (i.e.,~~
455 ~~Mediterranean) within the central California region. This evidence which along with the lack of~~
456 ~~change in average chain length (ACL) in the Lodo section (Fig S53) would suggest no major~~
457 ~~changes in vegetation assemblages during the PETM. knowledge As the uncertainty of using~~
458 ~~ACL as plant type change indicator combined with the model, about vegetation changes at~~
459 ~~certain level limits our ability to compute rainwater $\delta^2\text{H}$. Further~~ Another ~~factor~~
460 ~~reworking, under higher weathering rates during the PETM, deep weathering of Paleocene~~
461 ~~terrestrial *n*-alkanesorganic matter (e.g., Tipple et al., 2011), would could~~ possibly dampen of
462 isotopic *n*-alkane signals ~~deposited~~ at Lodo, ~~although the CPI and the leaf wax carbon isotopes~~
463 ~~would showssuggest minimal reworking organic matterof the *n*-alkanes, as opposed to other~~
464 ~~coastal PETM sitesregions- where the evidence for reworking is robust (e.g., Lyons et al., 2018).~~
465 ~~Nevertheless, i~~ As such, if we assume the $\delta^2\text{H}_{n\text{-alkane}}$ record reflects only on changes in ~~source~~
466 ~~local meteoric~~ waters, the observed modest change of $\delta^2\text{H}_{n\text{-alkane}}$ values at Lodo could be
467 interpreted in several ways ~~in terms of with respect to~~ T-related changes on isotope fractionations
468 ~~that were~~ offset by changes in dominant season of precipitation, and/or vapor sources and
469 distance of transport. For example, a shift in precipitation ~~seasonally~~ between winter and late
470 summer/fall could offset the effects of warming assuming a shift from a proximal (north or
471 central Pacific) to a more distal (Gulf of Mexico) source of vapor (Hu and Dominguez, 2015). At
472 ground level, stronger evapotranspiration during biosynthesis can isotopically be offset by
473 external water source availability (i.e. seasonal precipitation). Local/regional ground water table
474 variations caused by hydrological change would also affect the source water-use efficiency of
475 plants since surface water tends to be more depleted in some perennial species after intense
476 storms in the groundwater (Hou et al., 2008; Krishnan et al., 2014). Hydrogen isotope
477 fractionation in plants can also be biased by seasonal shift in regional vegetation growth regime.
478 For example, leaf wax lipids from terrestrial plants usually record hydrological conditions earlier

479 in the season rather than fully integrating the entire growing season (Hou et al., 2008; Tipple et
480 al., 2013). Finally, episodic extremes in precipitation may dominate the hydrogen isotopic
481 composition of the leaf wax (Krishnan et al., 2014). If ~~most~~ soil water is derived mainly from
482 extreme events during the growth season, the lack of a major shift in the Lodo $\delta^2\text{H}_{n\text{-alkane}}$ record
483 with the onset of the PETM changes might could reflect a combination effect of more ^2H -
484 depleted precipitation delivered by intensified seasonal storms with more ^2H -depleted
485 precipitation offset by warming induced ^2H -enrichment in leaf water.

486

487 4.3 Comparison of leaf water and modeled $\delta^2\text{H}$

488 Assuming the leaf waxes $\delta^2\text{H}$ are primarily influenced by local meteoric water, how does the
489 seasonal distribution of precipitation influence the bulk $\delta^2\text{H}$ signal in leaf waxes? In iCESM1.2
490 simulations with increasing $p\text{CO}_2$ (i.e., 3x to 6x pre-industry) and SST, the seasonal shifts in $\delta^2\text{H}$
491 of mean monthly precipitation from pre-PETM to PETM is significant. During the winter, as
492 precipitation amounts decline, Regional $\delta^2\text{H}_{\text{precip}}$ increases by 10‰ during wet winter while
493 decreasing by ~ 1 to 5‰ during late summer/fall in central California (Fig. 4). To estimate how
494 this seasonal change of $\delta^2\text{H}_{\text{precip}}$ and precipitation amount influences leaf water $\delta^2\text{H}$, we applied
495 a leaf wax proxy model (supplemental information) which computes the combined effects of
496 changes in seasonal precipitation and growing season length. The model shows leaf water $\delta^2\text{H}$
497 enriched ca. 4 to 7‰ from pre-PETM to PETM. consistent with $\delta^2\text{H}_{n\text{-alkane}}$ proxy record in Lodo
498 section. Arguably, this would be consistent with minor $\sim 65\%$ enrichment observed in the Lodo
499 record at the onset of the PETM. We also testexamined other sites for comparison of the
500 predicted leaf water differences from pre-PETM to PETM with the fossil leaf wax proxy
501 difference in $\Delta\delta^2\text{H}$ (see supplemental information), and find a similar pattern observed in other
502 mid-latitude sites. Therefore, this relatively muted leaf wax $\delta^2\text{H}_{n\text{-alkane}}$ response can be potentially
503 explained by a seasonal shift of heavy precipitation events. Alternatively Other factors to
504 consider include, precipitation source waters and a the change in leaf water $\delta^2\text{H}$ may also reflect
505 source water shift of a mixing endmember between proximal and distal sources of water in the
506 coast (Romero and Feakins, 2011). For example, with a summer shift of source water from the
507 Pacific to subtropics (i.e., summer monsoons), the effect of increasing distance and distillation
508 would isotopically deplete vapor (Hu and Dominguez, 2015), thus offsetting the temperature
509 related enrichment of local $\delta^2\text{H}_{\text{precip}}$. In addition, infrequent but high intensity tropical cyclones-

510 ~~induced heavy rainfall in the summer in mid-Pacific~~ during the PETM (Kiehl et al., 2021) ~~can~~
511 ~~also would tend to deliver relatively depleted~~ bring the precipitation ~~more depleted in hydrogen~~
512 ~~isotope~~ (i.e., a more negative $\delta^2\text{H}$) during summer months.

513
514 Finally, a related record that might indirectly reflect on precipitation amount (i.e., atmospheric
515 humidity) is the magnitude of the CIE as recorded by *n*-alkane leaf wax $\delta^{13}\text{C}_{n\text{-alkane}}$ ~~and~~
516 ~~magnitude of the CIE~~. Recalcitrant higher plants leaf wax *n*-alkane carbon isotope ratios ~~of long-~~
517 ~~chain *n*-alkane~~ ($n > 25$ with odd-over-even preference) reflect mainly carbon source (Diefendorf
518 et al., 2010). However, photosynthetic carbon isotope fractionation (Δ_p) is sensitive to
519 atmospheric $p\text{CO}_2$ variations, generally increase with rising concentrations assuming a constant
520 photosynthetic fractionation factor and humidity (Diefendorf et al., 2010). The $\delta^{13}\text{C}_{n\text{-alkane}}$ of
521 Lodo section displays a sharp negative shift of ca. 4 ‰ (average of $n\text{-C}_{27}$, $n\text{-C}_{29}$, $n\text{-C}_{31}$) across
522 the onset of CIE (Fig. 23b), which is consistent with global mean atmospheric CIE (Sluijs and
523 Dickens, 2012) but generally smaller than observed in other leaf wax records (Handley et al.,
524 2008, 2011; Jaramillo et al., 2010; Pagani et al., 2006; Tipple et al., 2011). The smaller $\delta^{13}\text{C}_{n\text{-$
525 $\text{alkane}}$ CIE recorded in Lodo could reflect on reduction in local humidity which preferentially
526 tends to reduce the magnitude of Δ_p during photosynthetic carbon fixation.

527 Summary and Conclusions

528
529
530 Many sections globally exhibit evidence, often striking, of significant shifts in local hydroclimate
531 at the onset of the PETM consistent with model simulations (e.g., 2x CO_2). These same models
532 also simulate

533 **5 Conclusion**

534 ~~With PETM greenhouse gas forcing (~56 Ma), climate simulations show~~ an overall decrease in
535 winter precipitation along for the central California margin coast due in large part to a reduction
536 in AR frequency (Shields et al., 2021), ~~whereas summer precipitation increases slightly. This is~~
537 generally consistent with the ~~o~~ While not as striking, the collection of observations from the
538 central California Lodo Gulch Section ~~based on various sedimentological and geochemical~~
539 ~~records, and thus~~ would support a modest reduction in precipitation (i.e. MAP) during the PETM
540 along with the possibility of an increase in the magnitude-frequency of extreme precipitation

541 events ~~during the PETM. This transition toward greater aridity and precipitation extremes is not~~
542 ~~unlike the forecasts for much of California over the coming centuries due to anthropogenic~~
543 ~~driven warming. In this regard, the observed hydroclimate response during the PETM as~~
544 ~~simulated in climate models in response to a doubling (or more) of CO₂ could serve as a past~~
545 ~~analog for potential hydroclimate changes in California.~~

546
547

548 Data availability. Data ~~tables of clay assemblages, grain size, organic carbon isotopes and leaf~~
549 ~~wax *n*-alkane stable isotopes~~ -will be available via the PANGAEA repository.

550
551 Author contribution. JCZ conceived the project ~~idea~~design, acquired funding and provided
552 overall supervision. XZ ~~conducted stable isotope measurements, clay mineralogy, grain size~~
553 ~~analyses and iCESM1.2/CAM5 model output analyses. Leaf wax *n*-alkane carbon and hydrogen~~
554 ~~isotope measurements were performed by BJT, WDR, JBN conducted leaf wax proxy model~~
555 ~~experiments and analyzed the results. JZ, CAS and WDR provide technical expertise~~
556 ~~in~~contributed to processing CAM5 model ~~simulation~~soutput. ~~This paper was prepared by XZ~~
557 ~~with a~~All authors contributed to the review and editing of the manuscript.

558
559 Competing interests. The authors declare that they have no conflict of interest.

560
561 Acknowledgements.
562 ~~We thank Colin Carney (UCSC SIL) for technical support and acknowledge the invaluable~~
563 ~~contributions of Dr. Mark Pagani (deceased).~~ Funding for this project has been provided by
564 National Science Foundation No. OCE 2103513 ~~to JCZ~~. All compound specific isotope analyses
565 were performed at the Yale Institute for Biospheric Studies-Earth Systems Center for Stable
566 Isotopic Studies that was supported by National Science Foundation Grant EAR 0628358 and
567 OCE 0902993. The CESM project is supported primarily by the National Science Foundation
568 (NSF). This material is based upon work supported by the National Center for Atmospheric
569 Research, which is a major facility sponsored by the NSF under Cooperative Agreement No.
570 1852977.

571
572

573 Reference:

574 Abell, J. T., Winckler, G., Anderson, R. F., and Herbert, T. D.: Poleward and weakened westerlies
575 during Pliocene warmth, *Nature*, 589, 70–75, <https://doi.org/10.1038/s41586-020-03062-1>, 2021.

576 [Blott, S. J., Croft, D. J., Pye, K., Saye, S. E., & Wilson, H. E. Particle size analysis by laser](#)
577 [diffraction. Geological Society, London, Special Publications, 232\(1\), 63-73, 2004.](#)

578 Brabb, E. E.: Studies in Tertiary stratigraphy of the California Coast Ranges., US Geological
579 Survey Professional Paper, 1213, 1983.

580 Brady, E., Stevenson, S., Bailey, D., Liu, Z., Noone, D., Nusbaumer, J., Otto-Bliesner, B. L., Tabor,
581 C., Tomas, R., Wong, T., Zhang, J., and Zhu, J.: The Connected Isotopic Water Cycle in the
582 Community Earth System Model Version 1, *J Adv Model Earth Syst*, 11, 2547–2566,
583 <https://doi.org/10.1029/2019MS001663>, 2019.

584 Büntgen, U., Urban, O., Krusic, P. J., Rybníček, M., Kolář, T., Kyncl, T., Ač, A., Koňasová, E.,
585 Čáslavský, J., Esper, J., Wagner, S., Saurer, M., Tegel, W., Dobrovlný, P., Cherubini, P.,
586 Reinig, F., and Trnka, M.: Recent European drought extremes beyond Common Era background
587 variability, *Nat Geosci*, 14, 190–196, <https://doi.org/10.1038/s41561-021-00698-0>, 2021.

588 [Campbell, J., Poulsen, C. J., Zhu, J., Tierney, J. E., and Keeler, J.: CO₂-driven and orbitally driven](#)
589 [oxygen isotope variability in the Early Eocene, *Clim. Past*, 20, 495–522,](#)
590 <https://doi.org/10.5194/cp-20-495-2024>, 2024.

591 Carmichael, M. J., Lunt, D. J., Huber, M., Heinemann, M., Kiehl, J., LeGrande, A., Loptson, C. A.,
592 Roberts, C. D., Sagoo, N., Shields, C., Valdes, P. J., Winguth, A., Winguth, C., and Pancost, R.
593 D.: A model-model and data-model comparison for the early Eocene hydrological cycle, *Climate*
594 *of the Past*, 12, 455–481, <https://doi.org/10.5194/CP-12-455-2016>, 2016.

595 Carmichael, M. J., Inglis, G. N., Badger, M. P. S., Naafs, B. D. A., Behrooz, L., Rimmelzwaal, S.,
596 Monteiro, F. M., Rohrssen, M., Farnsworth, A., Buss, H. L., Dickson, A. J., Valdes, P. J., Lunt,
597 D. J., and Pancost, R. D.: Hydrological and associated biogeochemical consequences of rapid
598 global warming during the Paleocene-Eocene Thermal Maximum,
599 <https://doi.org/10.1016/j.gloplacha.2017.07.014>, 1 October 2017.

600 [Cramwinckel, M. J., Burls, N. J., Fahad, A. A., Knapp, S., West, C. K., Reichgelt, T., ... & Inglis,](#)
601 [G. N. Global and zonal-mean hydrological response to early Eocene warmth. *Paleoceanography*](#)
602 [and *Paleoclimatology*, 38\(6\), e2022PA004542, 2023.](#)

603 Chen, C., Guerit, L., Foreman, B. Z., Hassenruck-Gudipati, H. J., Adatte, T., Honegger, L., Perret,
604 M., Sluijs, A., and Castellort, S.: Estimating regional flood discharge during Palaeocene-Eocene
605 global warming, *Sci Rep*, 8, 1–8, <https://doi.org/10.1038/s41598-018-31076-3>, 2018.

606 Diefendorf, A. F., Mueller, K. E., Wing, S. L., Koch, P. L., and Freeman, K. H.: Global patterns in
607 leaf ¹³C discrimination and implications for studies of past and future climate, *Proc Natl Acad*
608 *Sci U S A*, 107, 5738–5743, <https://doi.org/10.1073/pnas.0910513107>, 2010.

609 Douville, H., Raghavan, K., Renwick, J., and Allan, R.: Water Cycle Changes, Intergovernmental
610 Panel on Climate Change 2021 – The Physical Science Basis, 1055–1210,
611 <https://doi.org/10.1017/9781009157896.010>, 2021.

612 Foreman, B. Z.: Climate-driven generation of a fluvial sheet sand body at the Paleocene–Eocene
613 boundary in north-west Wyoming (USA), *Basin Research*, 26, 225–241,
614 <https://doi.org/10.1111/BRE.12027>, 2014.

615 Foreman, B. Z., Heller, P. L., and Clementz, M. T.: Fluvial response to abrupt global warming at
616 the Palaeocene/Eocene boundary, *Nature* 2012 491:7422, 491, 92–95,
617 <https://doi.org/10.1038/nature11513>, 2012.

618 Gibson, T. G., Bybell, L. M., and Mason, D. B.: Stratigraphic and climatic implications of clay
619 mineral changes around the Paleocene/Eocene boundary of the northeastern US margin,
620 *Sediment Geol*, 134, 65–92, [https://doi.org/10.1016/S0037-0738\(00\)00014-2](https://doi.org/10.1016/S0037-0738(00)00014-2), 2000.

621 Handley, L., Pearson, P. N., McMillan, I. K., and Pancost, R. D.: Large terrestrial and marine
622 carbon and hydrogen isotope excursions in a new Paleocene/Eocene boundary section from
623 Tanzania, *Earth Planet Sci Lett*, 275, 17–25, <https://doi.org/10.1016/j.epsl.2008.07.030>, 2008.

624 Handley, L., Crouch, E. M., and Pancost, R. D.: A New Zealand record of sea level rise and
625 environmental change during the Paleocene-Eocene Thermal Maximum, *Palaeogeogr*
626 *Palaeoclimatol Palaeoecol*, 305, 185–200, <https://doi.org/10.1016/j.palaeo.2011.03.001>, 2011.

627 Handley, L., O’Halloran, A., Pearson, P. N., Hawkins, E., Nicholas, C. J., Schouten, S., McMillan,
628 I. K., and Pancost, R. D.: Changes in the hydrological cycle in tropical East Africa during the
629 Paleocene-Eocene Thermal Maximum, *Palaeogeogr Palaeoclimatol Palaeoecol*, 329–330, 10–21,
630 <https://doi.org/10.1016/j.palaeo.2012.02.002>, 2012.

631 Held, I. M. and Soden, B. J.: Robust Responses of the Hydrological Cycle to Global Warming, *J*
632 *Clim*, 19, 5686–5699, <https://doi.org/10.1175/JCLI3990.1>, 2006.

633 Hou, J., D’Andrea, W. J., and Huang, Y.: Can sedimentary leaf waxes record D/H ratios of
634 continental precipitation? Field, model, and experimental assessments, *Geochim Cosmochim*
635 *Acta*, 72, 3503–3517, <https://doi.org/10.1016/j.gca.2008.04.030>, 2008.

636 Hu, H. and Dominguez, F.: Evaluation of Oceanic and Terrestrial Sources of Moisture for the North
637 American Monsoon Using Numerical Models and Precipitation Stable Isotopes, *J*
638 *Hydrometeorol*, 16, 19–35, <https://doi.org/10.1175/JHM-D-14-0073.1>, 2015.

639 Jaramillo, C., Ochoa, D., Contreras, L., Pagani, M., Carvajal-Ortiz, H., Pratt, L. M., Krishnan, S.,
640 Cardona, A., Romero, M., Quiroz, L., Rodriguez, G., Rueda, M. J., De La Parra, F., Morón, S.,
641 Green, W., Bayona, G., Montes, C., Quintero, O., Ramirez, R., Mora, G., Schouten, S.,
642 Bermudez, H., Navarrete, R., Parra, F., Alvarán, M., Osorno, J., Crowley, J. L., Valencia, V., and
643 Vervoort, J.: Effects of rapid global warming at the paleocene-eocene boundary on neotropical
644 vegetation, *Science* (1979), 330, 957–961, <https://doi.org/10.1126/science.1193833>, 2010.

645 John, C. M., Bohaty, S. M., Zachos, J. C., Sluijs, A., Gibbs, S., Brinkhuis, H., and Bralower, T. J.:
646 North American continental margin records of the Paleocene-Eocene thermal maximum:
647 Implications for global carbon and hydrological cycling, *Paleoceanography*, 23,
648 <https://doi.org/10.1029/2007PA001465>, 2008.

649 Kemp, S. J., Ellis, M. A., Mountney, I., and Kender, S.: Palaeoclimatic implications of high-
650 resolution clay mineral assemblages preceding and across the onset of the Palaeocene–Eocene
651 Thermal Maximum, North Sea Basin, *Clay Miner*, 51, 793–813,
652 <https://doi.org/10.1180/CLAYMIN.2016.051.5.08>, 2016.

653 Kiehl, J. T. and Shields, C. A.: Sensitivity of the palaeocene-eocene thermal maximum climate to
654 cloud properties, *Philosophical Transactions of the Royal Society A: Mathematical, Physical and*
655 *Engineering Sciences*, 371, <https://doi.org/10.1098/rsta.2013.0093>, 2013.

656 Kiehl, J. T., Shields, C. A., Snyder, M. A., Zachos, J. C., and Rothstein, M.: Greenhouse- and
657 orbital-forced climate extremes during the early Eocene, *Philosophical Transactions of the Royal*
658 *Society A: Mathematical, Physical and Engineering Sciences*, 376,
659 <https://doi.org/10.1098/RSTA.2017.0085>, 2018.

660 Kiehl, J. T., Zarzycki, C. M., Shields, C. A., and Rothstein, M. V.: Simulated changes to tropical
661 cyclones across the Paleocene-Eocene Thermal Maximum (PETM) boundary, *Palaeogeogr*
662 *Palaeoclimatol Palaeoecol*, 572, 110421, <https://doi.org/10.1016/J.PALAEO.2021.110421>, 2021.

663 Korasidis, V. A., Wing, S. L., Shields, C. A., and Kiehl, J. T.: Global Changes in Terrestrial
664 Vegetation and Continental Climate During the Paleocene-Eocene Thermal Maximum,
665 *Paleoceanogr Paleoclimatol*, 37, <https://doi.org/10.1029/2021PA004325>, 2022.

666 Kozdon, R., Penman, D. E., Kelly, D. C., Zachos, J. C., Fournelle, J. H., and Valley, J. W.:
667 Enhanced Poleward Flux of Atmospheric Moisture to the Weddell Sea Region (ODP Site 690)
668 During the Paleocene-Eocene Thermal Maximum, *Paleoceanogr Paleoclimatol*, 35, 1–14,
669 <https://doi.org/10.1029/2019pa003811>, 2020.

670 Kraus, M. J. and Riggins, S.: Transient drying during the Paleocene-Eocene Thermal Maximum
671 (PETM): Analysis of paleosols in the bighorn basin, Wyoming, *Palaeogeogr Palaeoclimatol*
672 *Palaeoecol*, 245, 444–461, <https://doi.org/10.1016/j.palaeo.2006.09.011>, 2007.

673 Krishnan, S., Pagani, M., Huber, M., and Sluijs, A.: High latitude hydrological changes during the
674 Eocene Thermal Maximum 2, *Earth Planet Sci Lett*, 404, 167–177,
675 <https://doi.org/10.1016/j.epsl.2014.07.029>, 2014.

676 Liu, B., Yan, Y., Zhu, C., Ma, S., and Li, J.: Record-Breaking Meiyu Rainfall Around the Yangtze
677 River in 2020 Regulated by the Subseasonal Phase Transition of the North Atlantic Oscillation,
678 *Geophys Res Lett*, 47, <https://doi.org/10.1029/2020GL090342>, 2020.

679 Massoud, E. C., Espinoza, V., Guan, B., and Waliser, D. E.: Global Climate Model Ensemble
680 Approaches for Future Projections of Atmospheric Rivers, *Earths Future*, 7, 1136–1151,
681 <https://doi.org/10.1029/2019EF001249>, 2019.

682 McInerney, F. A. and Wing, S. L.: The Paleocene-Eocene Thermal Maximum: A Perturbation of
683 Carbon Cycle, Climate, and Biosphere with Implications for the Future, *Annu Rev Earth Planet*
684 *Sci*, 39, 489–516, <https://doi.org/10.1146/annurev-earth-040610-133431>, 2011.

685 Nicolo, M. J., Dickens, G. R., and Hollis, C. J.: South Pacific intermediate water oxygen depletion
686 at the onset of the Paleocene-Eocene thermal maximum as depicted in New Zealand margin
687 sections, *Paleoceanography*, 25, 1–12, <https://doi.org/10.1029/2009PA001904>, 2010.

688 Pagani, M., Pedentchouk, N., Huber, M., Sluijs, A., Schouten, S., Brinkhuis, H., Damsté, J. S. S.,
689 Dickens, G. R., Backman, J., Clemens, S., Cronin, T., Eynaud, F., Gattacceca, J., Jakobsson, M.,
690 Jordan, R., Kaminski, M., King, J., Koc, N., Martinez, N. C., McInroy, D., Moore, T. C.,
691 O'Regan, M., Onodera, J., Pälike, H., Rea, B., Rio, D., Sakamoto, T., Smith, D. C., St John, K.
692 E. K., Suto, I., Suzuki, N., Takahashi, K., Watanabe, M., and Yamamoto, M.: Arctic hydrology
693 during global warming at the Palaeocene/Eocene thermal maximum, *Nature*, 442, 671–675,
694 <https://doi.org/10.1038/nature05043>, 2006.

695 [Peters, K.E., Walters, C.C., Moldowan, J.M., 2005. The Biomarker Guide: II Biomarkers](#)
696 [and Isotopes in Petroleum Systems and Earth History, 2nd edition. Cambridge Uni-](#)
697 [versity Press, Cambridge.](#)

698 [Polade, S. D., Gershunov, A., Cayan, D. R., Dettinger, M. D., and Pierce, D. W.: Precipitation in a](#)
699 [warming world: Assessing projected hydro-climate changes in California and other](#)
700 [Mediterranean climate regions OPEN, *Sci Rep*, 7, <https://doi.org/10.1038/s41598-017-11285-y>,](#)
701 [2017.](#)

702 Risser, M. D. and Wehner, M. F.: Attributable Human-Induced Changes in the Likelihood and
703 Magnitude of the Observed Extreme Precipitation during Hurricane Harvey, *Geophys Res Lett*,
704 44, 12,457–12,464, <https://doi.org/10.1002/2017GL075888>, 2017.

705 Romero, I. C. and Feakins, S. J.: Spatial gradients in plant leaf wax D/H across a coastal salt marsh
706 in southern California, *Org Geochem*, 42, 618–629,
707 <https://doi.org/10.1016/J.ORGGEOCHEM.2011.04.001>, 2011.

708 Rush, W. D., Kiehl, J. T., Shields, C. A., and Zachos, J. C.: Increased frequency of extreme
709 precipitation events in the North Atlantic during the PETM: Observations and theory,
710 *Palaeogeogr Palaeoclimatol Palaeoecol*, 568, <https://doi.org/10.1016/j.palaeo.2021.110289>,
711 2021.

712 Sachse, D., Billault, I., Bowen, G. J., Chikaraishi, Y., Dawson, T. E., Feakins, S. J., Freeman, K. H.,
713 Magill, C. R., McInerney, F. A., van der Meer, M. T. J., Polissar, P., Robins, R. J., Sachs, J. P.,
714 Schmidt, H.-L., Sessions, A. L., White, J. W. C., West, J. B., and Kahmen, A.: Molecular
715 Paleohydrology: Interpreting the Hydrogen-Isotopic Composition of Lipid Biomarkers from
716 Photosynthesizing Organisms, *Annu Rev Earth Planet Sci*, 40, 221–249,
717 <https://doi.org/10.1146/annurev-earth-042711-105535>, 2012.

718 Schmitz, B. and Pujalte, V.: Sea-level, humidity, and land-erosion records across the initial Eocene
719 thermal maximum from a continental-marine transect in northern Spain, *Geology*, 31, 689–692,
720 <https://doi.org/10.1130/G19527.1>, 2003.

721 Self-Trail, J. M., Robinson, M. M., Bralower, T. J., Sessa, J. A., Hajek, E. A., Kump, L. R.,
722 Trampush, S. M., Willard, D. A., Edwards, L. E., Powars, D. S., and Wandless, G. A.: Shallow
723 marine response to global climate change during the Paleocene-Eocene Thermal Maximum,
724 Salisbury Embayment, USA, *Paleoceanography*, 32, 710–728,
725 <https://doi.org/10.1002/2017PA003096>, 2017.

726 Shields, C. A. and Kiehl, J. T.: Atmospheric river landfall-latitude changes in future climate
727 simulations, *Geophys Res Lett*, 43, 8775–8782, <https://doi.org/10.1002/2016GL070470>, 2016.

728 Shields, C. A., Kiehl, J. T., Rush, W., Rothstein, M., and Snyder, M. A.: Atmospheric rivers in
729 high-resolution simulations of the Paleocene Eocene Thermal Maximum (PETM), *Palaeogeogr*
730 *Palaeoclimatol Palaeoecol*, 567, <https://doi.org/10.1016/j.palaeo.2021.110293>, 2021.

731 Simon Wang, S. Y., Yoon, J. H., Becker, E., and Gillies, R.: California from drought to deluge,
732 *Nature Climate Change* 2017 7:7, 7, 465–468, <https://doi.org/10.1038/nclimate3330>, 2017.

733 Slotnick, B. S., Dickens, G. R., Nicolo, M. J., Hollis, C. J., Crampton, J. S., Zachos, J. C., and
734 Sluijs, A.: Large-amplitude variations in carbon cycling and terrestrial weathering during the
735 latest Paleocene and earliest Eocene: The record at Mead Stream, New Zealand, *Journal of*
736 *Geology*, 120, 487–505, <https://doi.org/10.1086/666743>, 2012.

737 Sluijs, A. and Brinkhuis, H.: A dynamic climate and ecosystem state during the Paleocene-Eocene
738 Thermal Maximum: Inferences from dinoflagellate cyst assemblages on the New Jersey Shelf,
739 *Biogeosciences*, 6, 1755–1781, <https://doi.org/10.5194/bg-6-1755-2009>, 2009.

740 Sluijs, A. and Dickens, G. R.: Assessing offsets between the $\delta^{13}\text{C}$ of sedimentary components and
741 the global exogenic carbon pool across early Paleogene carbon cycle perturbations, *Global*
742 *Biogeochem Cycles*, 26, <https://doi.org/10.1029/2011GB004224>, 2012.

743 Sluijs, A., Brinkhuis, H., Crouch, E. M., John, C. M., Handley, L., Munsterman, D., Bohaty, S. M.,
744 Zachos, J. C., Reichert, G. J., Schouten, S., Pancost, R. D., Damsté, J. S. S., Welters, N. L. D.,
745 Lotter, A. F., and Dickens, G. R.: Eustatic variations during the Paleocene-Eocene greenhouse
746 world, *Paleoceanography*, 23, <https://doi.org/10.1029/2008PA001615>, 2008.

747 Smith, F. A., Wing, S. L., and Freeman, K. H.: Magnitude of the carbon isotope excursion at the
748 Paleocene-Eocene thermal maximum: The role of plant community change, *Earth Planet Sci*
749 *Lett*, 262, 50–65, <https://doi.org/10.1016/j.epsl.2007.07.021>, 2007.

750 Stassen, P., Thomas, E., and Speijer, R. P.: The progression of environmental changes during the
751 onset of the Paleocene-Eocene thermal maximum (New Jersey coastal plain), *Austrian Journal of*
752 *Earth Sciences*, 105, 169–178, 2012.

753 Stevenson, S., Coats, S., Touma, D., Cole, J., Lehner, F., Fasullo, J., and Otto-Bliesner, B.: Twenty-
754 first century hydroclimate: A continually changing baseline, with more frequent extremes,
755 PNAS, 119, <https://doi.org/10.1073/pnas>, 2022.

756 Swain, D. L., Langenbrunner, B., Neelin, J. D., and Hall, A.: Increasing precipitation volatility in
757 twenty-first-century California, *Nat Clim Chang*, 8, 427–433, <https://doi.org/10.1038/s41558-018-0140-y>, 2018.

759 Tateo, F.: Clay minerals at the paleocene–eocene thermal maximum: Interpretations, limits, and
760 perspectives, *Minerals*, 10, 1–16, <https://doi.org/10.3390/min10121073>, 2020.

761 Tipple, B. J., Pagani, M., Krishnan, S., Dirghangi, S. S., Galeotti, S., Agnini, C., Giusberti, L., and
762 Rio, D.: Coupled high-resolution marine and terrestrial records of carbon and hydrologic cycles
763 variations during the Paleocene – Eocene Thermal Maximum (PETM), *Earth Planet Sci Lett*,
764 311, 82–92, <https://doi.org/10.1016/j.epsl.2011.08.045>, 2011.

765 Tipple, B. J., Berke, M. A., Doman, C. E., Khachatryan, S., and Ehleringer, J. R.: Leaf-wax n-
766 alkanes record the plant-water environment at leaf flush, *Proc Natl Acad Sci U S A*, 110, 2659–
767 2664, <https://doi.org/10.1073/pnas.1213875110>, 2013.

768 Tipple, B. J., Berke, M. A., Hambach, B., Roden, J. S., and Ehleringer, J. R.: Predicting leaf wax n-
769 alkane 2H/1H ratios: controlled water source and humidity experiments with hydroponically
770 grown trees confirm predictions of Craig–Gordon model, *Plant Cell Environ*, 38, 1035–1047,
771 <https://doi.org/10.1111/PCE.12457>, 2015.

772 Vogel, M. M., Hauser, M., and Seneviratne, S. I.: Projected changes in hot, dry and wet extreme
773 events’ clusters in CMIP6 multi-model ensemble, *Environmental Research Letters*, 15,
774 <https://doi.org/10.1088/1748-9326/ab90a7>, 2020.

775 Wakeham, S. G. and Pease, T. K.: Lipid Analysis in Marine Particle and Sediment Samples A
776 Laboratory Handbook, 2004.

777 ~~de Wet, C. B., Erhardt, A. M., Sharp, W. D., Marks, N. E., Bradbury, H. J., Turchyn, A. V., Xu, Y.,
778 and Oster, J. L.: Semiquantitative Estimates of Rainfall Variability During the 8.2 kyr Event in
779 California Using Speleothem Calcium Isotope Ratios, <https://doi.org/10.1029/2020GL089154>,
780 16 February 2021.~~

781 Williams, A. P., Cook, E. R., Smerdon, J. E., Cook, B. I., Abatzoglou, J. T., Bolles, K., Baek, S. H.,
782 Badger, A. M., and Livneh, B.: Large contribution from anthropogenic warming to an emerging
783 North American megadrought, *Science* (1979), 368, 314–318, 2020.

784 Willis, K.J, McElwain, J. C.: *The Evolution of Plants*, OUP Oxford, 392 pp., 2002.

785 Wing, S. L., Harrington, G. J., Smith, F. a, Bloch, J. I., Boyer, D. M., and Freeman, K. H.: Transient
786 Floral Change and rapid global warming at the P/E boundary, *Science* (1979), 310, 993–996,
787 <https://doi.org/10.1126/science.1116913>, 2005.

788 Zachos, J. C., Dickens, G. R., and Zeebe, R. E.: An early Cenozoic perspective on greenhouse
789 warming and carbon-cycle dynamics, *Nature*, 451, 279–283,
790 <https://doi.org/10.1038/nature06588>, 2008.

791 ~~Zamora-Reyes, D., Broadman, E., Bigio, E., Black, B., Meko, D., Woodhouse, C. A., and Trouet,
792 V.: The Unprecedented Character of California’s 20th Century Enhanced Hydroclimatic
793 Variability in a 600 Year Context, *Geophys Res Lett*, 49,
794 <https://doi.org/10.1029/2022GL099582>, 2022.~~

795 Zhu, J., Poulsen, C. J., Otto-Bliesner, B. L., Liu, Z., Brady, E. C., and Noone, D. C.: Simulation of
796 early Eocene water isotopes using an Earth system model and its implication for past climate
797 reconstruction, *Earth Planet Sci Lett*, 537, 116164, <https://doi.org/10.1016/j.epsl.2020.116164>,
798 2020.

799 Zscheischler, J. and Lehner, F.: Attributing Compound Events to Anthropogenic Climate Change,
800 Bull Am Meteorol Soc, 103, E936–E953, <https://doi.org/10.1175/BAMS-D-21-0116.1>, 2022.

801

802